Journal of Materials Chemistry C

ROYAL SOCIETY OF CHEMISTRY

PAPER

Cite this: J. Mater. Chem. C, 2021, 9, 7713

A highly stable, selective, and high-performance VOC sensor using a SnS_2 nano-lotus structure†

Rajneesh Kumar Mishra, [a] Gyu Jin Choi,[a] Yogendra Kumar Mishra, [b] Ajeet Kaushik, [c] Youngku Sohn,[d] Seung Hee Lee *[e] and Jin Seog Gwag *[a]

This research demonstrates the design and development of a novel SnS_2 nano-lotus structure (NLS) using a one-step eco-friendly solvothermal method which can detect volatile organic compounds (VOCs) and involves a 3-S approach, *i.e.*, obtaining stability, sensitivity, and selectivity. As a unique feature, the UV-visible spectroscopy results showed an optical band gap of 2.25 eV and Urbach energy states at 630, 675, 751, and 793 meV. Thus, a gas sensing mechanism that is correlated with the optical band gap and Urbach energy states of SnS_2 NLS, leading to selectivity with reference to a targeted VOC, is discussed in this research. This SnS_2 NLS sensor demonstrates the highest response (sensitivity) of 93.5% to 25 ppm ethanol at 90 °C, compared with its responses to methanol (16.6%), propanol (14.8%), and *n*-butanol (11.4%). The SnS_2 NLS sensor for ethanol shows rapid response (14.2 s) and quick recovery (16.6 s) times toward a concentration of 25 ppm at 90 °C. The SnS_2 NLS sensor demonstrates better selectivity towards ethanol, with the response of 92.9% being much higher compared to its responses to other interfering gases, such as methanol (16.4%), propanol (14.8%), *n*-butanol (11.4%), benzene (4.1%), toluene (5.8%), and *n*-butylacetate (2.2%). The value of the selectivity coefficient with respect to *n*-butylacetate is high, 34.5, which indicates that the SnS_2 NLS sensor response to ethanol is 34.5 times higher than the response to *n*-butylacetate. However, the value of the selectivity coefficient towards methanol is low, 4.3, which shows that the SnS_2 NLS sensor response to ethanol is only 4.3 times higher than the response to methanol. In addition to selectivity, the SnS_2 NLS sensor displays outstanding stability, with a response of 91.3% after 25 days (tested at 5 day intervals) to a concentration of 25 ppm ethanol at 90 °C. The SnS_2 NLS sensor exhibits a theoretical detection limit of 7.9 ppb toward ethanol at 90 °C. Taking the sensing outcomes into consideration, the unique SnS_2 NLS VOC sensor with tunable performance can be projected to act as an analytical tool to detect a category of VOCs efficiently.

Received 8th February 2021,
Accepted 21st May 2021

DOI: 10.1039/d1tc00615k

rsc.li/materials-c

Introduction

The levels of environmentally hazardous volatile organic compound (VOC) molecules are increasing continuously in the modern world due to rapid growth in the agriculture, transport, and industrial sectors. The unwanted introduction of VOCs can affect health and bodily function, causing several severe health conditions.[1] VOCs can be categorized into different groups, such as oxyhydrocarbons, aromatic hydrocarbons, aliphatic hydrocarbons, halogenated hydrocarbons, aldehydes, esters, and terpenes.[2,3] VOCs are the most commonly used chemicals in households and industry, being used in areas such as air fresheners, food fermentation, perfumes, wood preservatives, and disinfectants, hugely contributing to indoor air pollution.[4] VOCs, especially methanol (CH_3OH), ethanol (C_2H_5OH), propanol [$CH_3(CH_2)_2OH$], and *n*-butanol (C_4H_9OH), are extremely harmful because of their low boiling points and narcotic nature, and they can damage eyes and the respiratory system, cause fatigue, headaches, nausea, and vomiting, and irritate the skin.[5–7] A related issue is that exhaled human breath comprises more than 3500 components; of these, almost 50% of the components are from inhaled breath, such as nitrogen, oxygen, water vapor, carbon dioxide,[7] and a mixture of VOCs,

[a] Department of Physics, Yeungnam University, Gyeongsan, Gyeongbuk, 38541, South Korea. E-mail: sweat3000@ynu.ac.kr
[b] Mads Clausen Institute, NanoSYD, University of Southern Denmark, Alsion 2, 6400, Sønderborg, Denmark
[c] NanoBioTech Laboratory, Department of Natural Sciences, Division of Sciences, Arts & Mathematics, Florida Polytechnic University, Lakeland, FL, 33805-8531, USA
[d] Department of Chemistry, Chungnam National University, Daejeon, 34134, South Korea
[e] Information Display/Energy Laboratory, Department of Nanoconvergence Engineering and Department of Polymer Nano-Science and Technology, Jeonbuk (Chonbuk) National University, Jeonju, Jeonbuk 54896, South Korea. E-mail: lsh1@jbnu.ac.kr

† Electronic supplementary information (ESI) available. See DOI: 10.1039/d1tc00615k

like acetone, ethanol, propanol, and toluene.[8] Therefore, reliable, quick, highly selective, and stable gas sensors showing the 3-S features (stability, sensitivity, and selectivity) are in high demand for the real-time monitoring of VOCs in indoor environments, as well as for preventing drunk driving, which is especially desirable. In addition, they can be utilized as analytical tools, where VOCs serve as markers for efficient disease diagnosis.[9] However, obtaining fast response/recovery times, high responses, and long-lasting materials are colossal challenges to be overcome. The crucial parameters for gas sensor materials are high surface areas and morphologies that can interact quickly with gas molecules, cost-effectiveness, eco-friendliness, and excellent conductivity. To develop efficient gas sensors for selective VOC detection applications, various types of metal-oxide-based gas sensors have been investigated.

Currently, transition metal dichalcogenides (TMDs) have gained widespread attention because of their adjustable bandgaps and excellent electrical and optical properties.[10] Among them, SnS_2 is emerging as an exceptional two-dimensional, n-type (IV–VI) semiconducting material with a versatile bandgap, suitable electronegativity, and decent oxidation resistance.[11,12] SnS_2 has a hexagonal CdI_2-type crystal structure comprising S–Sn–S triple layers with weak van der Waals forces, allowing it to form stable structures with few atomic layers.[13,14] Interestingly, SnS_2 demonstrated excellent gas-sensing performance due to its highly adsorptive nature and high thermal stability (up to 300 °C).[15] Pure SnS_2 nanostructures and heterostructures have been studied for gas sensor applications to detect different kinds of gas molecules. However, few reports have been given in the literature relating to VOC sensing. Sun *et al.* discussed a SnS_2/SnS p–n heterojunction based NO_2 sensor, which demonstrated a sensing response of 660% at a concentration of 4 ppm at room temperature.[15] Bharatula *et al.* studied a SnS_2 nanoflake based alcohol (methanol, ethanol, and isopropyl alcohol) sensor.[16] The SnS_2 nanoflake sensor showed a higher response (1580) to methanol than to ethanol (<300) and isopropyl alcohol (<150) at a concentration of 150 ppm at 25 °C. Zhang *et al.* investigated a SnS/SnS_2 nanoparticle based ethanol sensor, which shows an excellent sensing response of below 80 in response to a concentration of 1000 ppm at 200 °C.[17] Shan *et al.* examined the ethanol detecting characteristics when using SnS as a gas sensing material.[18] The SnS gas sensor exhibited a high gas sensing response of 14.86 to a concentration of 100 ppm at 150 °C. Kuchi *et al.* fabricated a PbS/SnS_2 nanocomposite sensor, which showed a high gas sensing response of 100.3 to an ethanol concentration of 1600 ppm at room temperature.[19] The above-discussed research is only focused on SnS_2 heterostructure based gas sensors for target gas molecule detection. However, these reports do not sufficiently explore advancements and mechanisms related to the Urbach energy states in the bandgap of SnS_2 or provide comparative studies of VOC molecule sensing.

In this work, we synthesize a novel SnS_2 nano-lotus structure (NLS) using a single-step solvothermal method. Robust SnS_2 NLS, with the high capability to stimulate the charge transfer rate, offers the rapid and selective sensing of VOCs with improved response and recovery times. The present SnS_2 NLS sensor has been tested toward methanol, ethanol, propanol, and *n*-butanol at different temperatures (30–150 °C) and various concentrations (5–25 ppm). Further, the sensing characteristics are investigated and discussed in detail. In addition, the SnS_2 NLS gas sensor manifests excellent selectivity toward ethanol molecules in the presence of diverse VOCs (to be specific, methanol, propanol, *n*-butanol, benzene, toluene, and *n*-butylacetate) at a concentration of 25 ppm at 90 °C. Moreover, the SnS_2 NLS gas sensor manifests noticeable endurance for up to thirty days, with measurements taken every two days, in terms of its response to an ethanol concentration of 25 ppm at 90 °C. An optical bandgap study harmonized with an investigation of the Urbach energy states in SnS_2 NLS exhibits their prominent role in VOC sensing, which is discussed in detail.

Experimental procedure

Materials and synthesis

Tin tetrachloride pentahydrate ($SnCl_4{\cdot}5H_2O$) and thioacetamide (C_2H_5NS) were obtained from Sigma Aldrich. Isopropyl alcohol and ethanol were obtained from Merck. All chemicals were used as received.

The synthesis process and an atomic visualization of the crystallographic information are illustrated in Scheme 1. Tin tetrachloride pentahydrate (0.54 g) was dissolved in a mixture of isopropyl alcohol and deionized water (DI water) (75 mL : 5 mL) under magnetic stirring. After that, thioacetamide (0.59 g) was added to the prepared tin precursor solution and mixed well to form a uniform solution. The prepared tin/thioacetamide precursor mixture was added to a 100 mL autoclave. The autoclave was kept for 24 h in an oven at 180 °C and, after that, it was cooled naturally to room temperature. The synthesized material (powder form) was cleaned many times using ethanol and DI water, completely dehydrated under vacuum at 75 °C (5 h), and annealed at 200 °C for 2 h. Further, the SnS_2 nano-lotus structure (NLS) was collected as the final product.

Characterization

X-Ray diffraction (XRD) data was investigated using PANalytical apparatus with Cu K_α radiation. XRD provides insights into the crystal structure, crystallite size, lattice parameters, lattice spacing, and lattice strain of SnS_2 NLS. Raman spectroscopy studies are also carried out to investigate the structural properties of SnS_2 NLS using a spectrophotometer (Horiba JOBIN YVON, Lab RAM HR) at 532 nm. XPS (X-ray photoelectron spectroscopy) was implemented to study the elements in SnS_2 NLS using an Al K-alpha 400 μm X-ray source (Thermo Scientific, UK). TEM (transmission electron microscopy) and FESEM (field-emission electron microscopy) studies were carried out to examine the shape, structure, and elemental composition of SnS_2 NLS. FESEM (S-4800, HITACHI Ltd, Japan) was used to investigate the morphology and thickness of SnS_2 NLS and to obtain color mapping of the Sn and S elements. TEM (JEOL JEM 2100F) was used to study the morphology, particle size, and lattice spacing of SnS_2 NLS and to obtain color mapping of the Sn and S elements. UV-vis diffuse reflectance spectroscopy (UV-vis-DRS)

Scheme 1 Schematic representations of SnS_2 NLS synthesis, crystal structure visualization, and sensor device fabrication.

data were recorded using a Scinco spectrophotometer (SCINCO Co. Ltd, South Korea). The Brunauer–Emmett–Teller (BET) specific surface area and Barrett–Joyner–Halenda (BJH) pore size and pore volume data were obtained using Physisorption Analyzer BET apparatus (Micromeritics) with an analysis bath temperature of 77.3 K after degassing at 200 °C for 24 h.

Gas sensor fabrication and measurements

The gas sensor was fabricated *via* the following method: (i) SnS_2 NLS was deposited on a glass slide *via* drop-casting and, after that, it was made into a rectangular shape using Scotch tape (dried at 90 °C for 8 h); and (ii) Ag electrodes were deposited using a paintbrush on both sides of the SnS_2 NLS film, as shown in Fig. S1 (ESI†). Volatile organic compound (VOC) sensing measurements using the gas sensor based on the SnS_2 NLS sensing material were carried out at several gas concentrations and operating temperatures. The VOC gas sensing measurements were conducted under ambient conditions. First, the SnS_2 sensor (Fig. S1, ESI†) was placed in the testing chamber (Fig. S2, ESI†). It was then subjected to the working temperature for 20 min to stabilize the sensor. Second, when the gas sensor working temperature reached the required value and stability was obtained, measurements were recorded before and after VOC insertion into the testing chamber. The temperature near the surface of the SnS_2 NLS gas sensor was monitored using a digital multimeter (Motwane-454). The electrical resistance of the SnS_2 NLS gas sensor was measured using a 6-1/2-digit digital multimeter (Keithley-2100). The VOC (methanol, ethanol, propanol, and *n*-butanol) concentrations were obtained *via* using the required amounts of liquid VOCs (eqn (S1), ESI†), and a Hamilton microsyringe was used to inject them into the homemade gas testing furnace at different operating temperatures. The synthesis process, an atomic visualization of SnS_2 crystallographic information, and the sensor device fabrication process are represented in Scheme 1.

Results and discussion

Structure, elements, and morphology

Scheme 1 presents the synthesis of SnS_2 NLS, crystallographic views, and the sensor device fabrication process using the SnS_2 nano-lotus structure (NLS). Detailed synthesis and sensor device fabrication procedures are described in the appropriate sections of the experimental procedure given above. The morphology and elemental composition of as-synthesized SnS_2 NLS are studied *via* FESEM, and data are shown in Fig. 1. Fig. 1(a) depicts an FESEM image of SnS_2 NLS, which shows the consistent growth of the nano-lotus structure. Fig. 1(b) and (c) shows an illustration of the lotus leaves and petals of SnS_2 NLS,

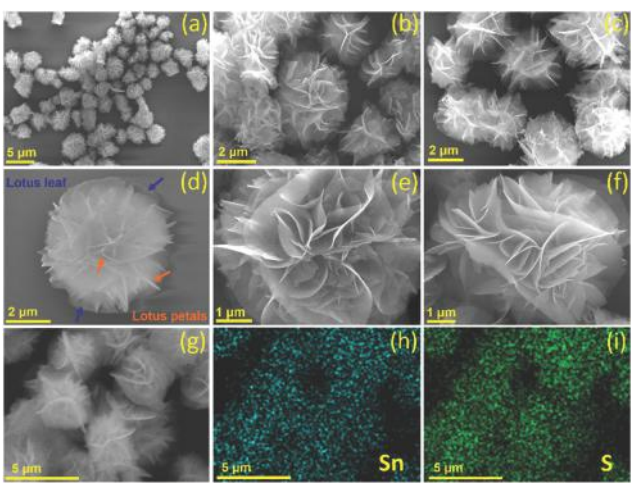

Fig. 1 FESEM analysis: (a) the uniform distribution of the nano-lotus structure; (b and c) the identification of nano-lotus leaves and petals; (d) an illustration of a single nano-lotus structure; (e and f) differently sized nano-lotus petals and their thickness; and (g) the selected area for the color mapping of (h) Sn and (i) S elements in SnS_2 NLS.

without the presence of any other differently sized particles/shapes. Fig. 1(d) shows a top view of a single SnS_2 NLS particle, demonstrating identical nano-lotus leaves and petals. Fig. 1(e) and (f) divulges that the petal sizes range from 5 nm to 50 nm. It is considered that the differently sized petals assemble to form SnS_2 NLS. The gaps between the SnS_2 NLS petals allow the formation of ionic active sites (O_x^-) and superior charge transfer rates during VOC sensing measurements. Fig. 1(g)–(i) shows a selected area and the corresponding elemental mapping of Sn and S elements, respectively.

Furthermore, the morphology, structure, and elemental composition of SnS_2 NLS were examined *via* TEM, HRTEM, and fast Fourier transform studies, and *via* atomic-resolution high-angle annular dark-field (HAADF) imaging with color mapping. Fig. 2(a) and (b) depicts the unique nanostructure of SnS_2 NLS with twisted, folded, and curved surfaces. Fig. 2(c) shows a high-magnification image, which illustrates the curved and cone-like twisted petal surfaces of SnS_2 NLS. These petal surfaces expose more surface area for the interaction of VOC molecules with the SnS_2 NLS sensor element. Fig. 2(d) shows a dark-field (HAADF) image that seems to be a top view of a single nano-lotus structure, further confirming the information seen in the FESEM image of SnS_2 NLS shown in Fig. 1(d). The estimated SnS_2 nano-lotus structure and petal size ranges are 2.8–3.2 μm and 3–40 nm, respectively, as shown in Fig. 2(a)–(d). To further study the microstructure of SnS_2 NLS, a high-resolution TEM image (HRTEM) is recorded, as shown in Fig. 2(e). From Fig. 2(e1) and (e2), the enlarged selected areas of the HRTEM image display a lattice spacing of around 0.59 nm, corresponding to the (001) lattice plane of SnS_2 NLS, which suitably matches the lattice spacing and planes of SnS_2 NLS observed *via* XRD (Fig. 3(a)). In addition, Fig. 2(e3) and (e4) illustrates FFT images corresponding to the (001) lattice plane revealed in the HRTEM images in Fig. 2(e1) and (e2). Fig. 2(f)–(h) shows a dark-field image and the corresponding elemental mapping of uniformly distributed Sn and S elements, further verifying the color mapping results from the FESEM study (Fig. 1(g)–(i)).

Fig. 3(a) depicts the XRD pattern of SnS_2 NLS, which matches the reference pattern of SnS_2 (JCPDS No. 23-0677). The XRD characteristic peaks located at 15.04°, 28.32°, 30.38°, 32.21°, 41.95°, 46.27°, 50.09°, 52.59°, 55.0°, 58.57°, 60.7°, and 63.16° correspond to the (001), (100), (002), (101), (102), (003), (110), (111), (103), (200), (201), and (004) Miller planes, respectively, of hexagonal SnS_2 NLS, and these match suitably with the reference pattern JCPDS No. 23-0677.[20] Fig. S3(a) (ESI†) shows the Rietveld refinement data from the XRD spectrum of SnS_2 NLS. The lattice spacing (d), lattice constants ($a = b$, and c), and lattice strain were evaluated using eqn (S2) (ESI†), the Rietveld refinement results, and eqn (S3) (ESI†), respectively, and the data are listed in Table S1 (ESI†). The lattice parameter ($a = b$, & c), c/a ratio, and average lattice strain (ε) values for SnS_2 NLS are 3.6438 Å ($a = b$), 5.9038 Å (c), 1.6202 (c/a), and 0.0055 (ε), which are comparable to the standard values (JCPDS No. 23-0677), as discussed in Table S1 (ESI†). However, it is observed that the XRD peaks are slightly shifted towards lower Bragg angles, which can be responsible for the existence of lattice strain. Fig. 3(b) depicts the Raman spectrum of SnS_2 NLS. Two characteristic Raman phonon bands are observed at 212.4 cm^{-1} and 321.6 cm^{-1}, corresponding to the E_g (in-plane) and A_{1g} (out-of-plane) vibrational phonon modes of SnS_2 NLS, respectively.[21] The optical Raman phonon mode A_{1g} arises due to the vertical plane

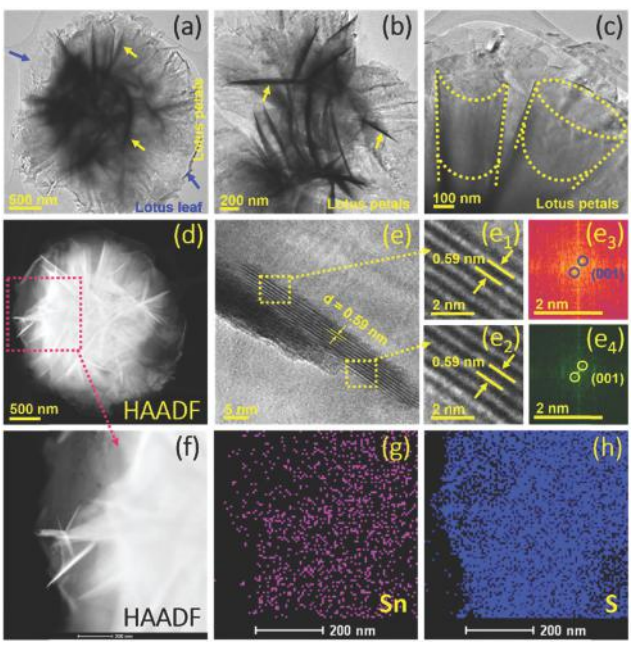

Fig. 2 FESEM images: (a) SnS_2 nano-lotus leaves and petals; (b) an illustration of SnS_2 nano-lotus petals; and (c) the curved and cone-like folding of SnS_2 nano-lotus petals. (d) A dark-field (HAADF) image of SnS_2 nano-lotus leaves and petals. (e) A HRTEM image of SnS_2 NLS, (e_1 and e_2) enlarged portions of the HRTEM image, and (e_3 and e_4) the corresponding FFT images. (f) A dark-field (HAADF) image for the color mapping of (g) Sn and (h) S elements of SnS_2 NLS.

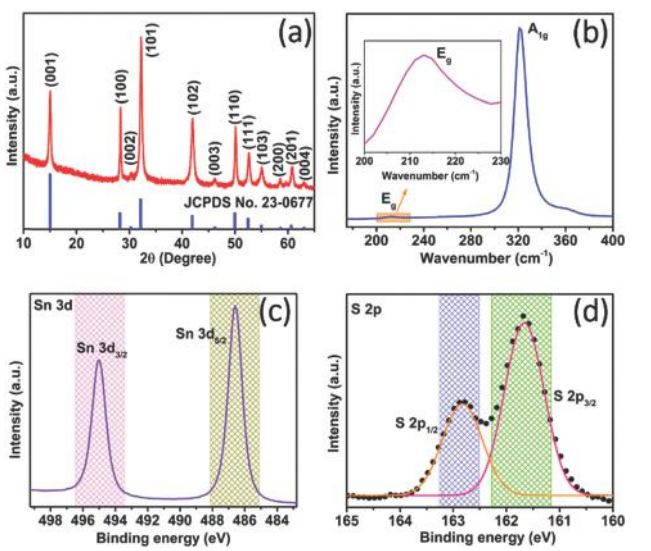

Fig. 3 (a) The XRD pattern (with the JCPDS No. 23-0677 standard pattern as blue lines), (b) the Raman spectrum (the inset shows the E_g band), and the narrow-scan XPS spectra of the (c) Sn 3d and (d) S 2p peak areas of SnS_2 NLS.

vibration of Sn–S bonds. The elemental composition and valence states of SnS_2 NLS were studied using XPS. Fig. S3(b) (ESI†) shows the XPS survey spectrum of SnS_2 NLS with Sn 4d, S 2p, S 2s, Sn 3d, and Sn 3p peaks at binding energies of 26.58 eV; 162.45 eV; 226.48 eV; 487.02 eV and 495.38 eV; and 716.54 eV and 758.47 eV, respectively. The Sn 3d and S 2p peaks are characteristics peaks of SnS_2 NLS, and they are observed at 487.02 eV and 495.38 eV, and 162.45 eV, respectively. Further, Fig. 3(c) and (d) elucidates the narrow scan spectra of the Sn 3d and S 2p characteristic peak areas, respectively. Fig. 3(c) displays the narrow-scan XPS spectrum of SnS_2 in the Sn 3d area, showing the manifestation of Sn $3d_{5/2}$ and Sn $3d_{3/2}$ characteristics peaks located at 486.56 eV and 495.04 eV, respectively, signifying the existence of the Sn^{4+} chemical state in SnS_2.[22] Further, Fig. 3(d) exhibits the narrow-scan XPS spectrum of SnS_2 in the S 2p area, divulging the appearance of two peaks at binding energy values of 161.66 eV and 162.83 eV, which are connected to the spin–orbit coupling of the characteristic S $2p_{3/2}$ and S $2p_{1/2}$ peaks, respectively, representing the S_2^{2-} chemical state in SnS_2.[22] These XRD, Raman, and XPS findings further authenticate the TEM and FESEM results, showing the fruitful development of hexagonal SnS_2 NLS. Further, the BET nitrogen adsorption–desorption and BJH methods were employed to study the porous nanostructure, and the results are shown in Fig. S4(a), (b) and in Table S2 (ESI†). The BET surface area of SnS_2 NLS is 10.2304 $m^2\ g^{-1}$, as shown in Fig. S4(a) and listed in Table S2 (ESI†). The pore size and pore volume of SnS_2 NLS, acquired *via* the BJH method, are 32.3905 nm and 0.0459 $cm^3\ g^{-1}$, respectively, as shown in Fig. S4(b) and listed in Table S2 (ESI†).

The UV-visible diffuse reflectance (DRS) absorption spectrum of SnS_2 NLS is obtained using a UV-visible DRS spectrometer to investigate the bandgap and Urbach energy states. Fig. S5 (ESI†) shows the UV-visible DRS absorption spectrum of SnS_2 NLS. The optical bandgap of SnS_2 NLS was evaluated using eqn (S4)–(S6), as discussed in the ESI,† and the absorbance spectrum, as shown in Fig. S5 (ESI†).[23,24] The optical bandgap of SnS_2 NLS, investigated using the linear region of the Tauc plot, as shown in Fig. 4(a), is 2.25 eV.

Moreover, the Urbach energy states can be evaluated using eqn (S4), (S7) and (S8), as discussed in the ESI.† Urbach energy states are usually described as the widths of the tails of localized energy states in the bandgap, which may be due to lattice strain.[25] Fig. 4(b) reveals plots of $\ln[F(R)]$ *vs.* the photon energy ($h\nu$) and the linear fitting lines used to unearth the Urbach energy states in the optical bandgap of SnS_2 NLS.[26] In Fig. 4(b), we selected four different energy ranges, 2.24–2.22 eV; 2.21–2.19 eV; 2.17–2.16 eV; and 2.14–2.13 eV, below the bandgap (2.25 eV) of SnS_2 NLS to calculate the Urbach energy state in each energy range. The slope of the fitting line in each energy range is the reciprocal of the Urbach energy, as discussed in eqn (S8) in the ESI.†[25,26] *Via* applying eqn (S8) (ESI†), the evaluated values of the Urbach energy states are 630 meV, 675 meV, 751 meV, and 793 meV for the energy ranges of 2.24–2.22 eV, 2.21–2.19 eV, 2.17–2.16 eV, and 2.14–2.13 eV, respectively. The inset of Fig. 4(a) shows a graphic sketch of the Urbach energy states below the conduction band of the bandgap of SnS_2 NLS. The Urbach energy states in the bandgap of SnS_2 NLS can play a crucial role in enabling faster analyte adsorption/desorption kinetics during VOC sensing.

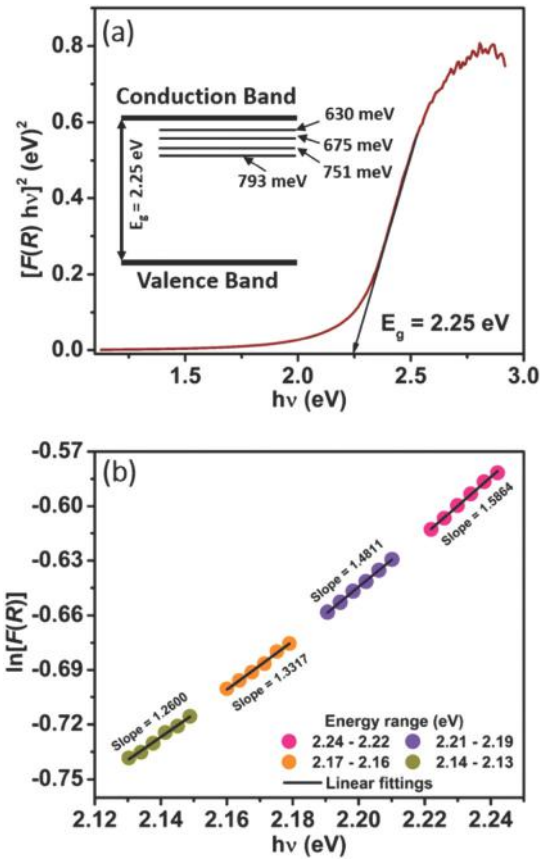

Fig. 4 (a) The optical bandgap and (b) calculations of the Urbach energy states in different energy regions below the conduction band of SnS_2 NLS.

Gas sensing properties

The SnS_2 NLS VOC sensor response is evaluated according to eqn (1):[27]

$$S = \frac{R_a - R_g}{R_a} \times 100\% \quad (1)$$

where S, R_a, and R_g are the response, sensor resistance in air, and sensor resistance in response to a VOC, respectively. The response of a gas sensor is a vital parameter that is greatly affected by the operating temperature, and the presence of electrons in/below the conduction band is crucial, as they can play a pivotal role in reacting with atmospheric oxygen to form active sites (O_x^-). In order to optimize the working temperature of the SnS_2 NLS VOC sensor, the responses toward methanol, ethanol, propanol, and *n*-butanol (VOCs) at different concentrations (5–25 ppm) and different operating temperatures (30–150 °C) were meticulously investigated. The response of the SnS_2 NLS VOC sensor enormously depends on the electron mobility,[28] semiconductor bandgap, Urbach energy states (defect energy states in the optical bandgap), test gas concentration, lattice defects, electrical conductivity,[28] and operating

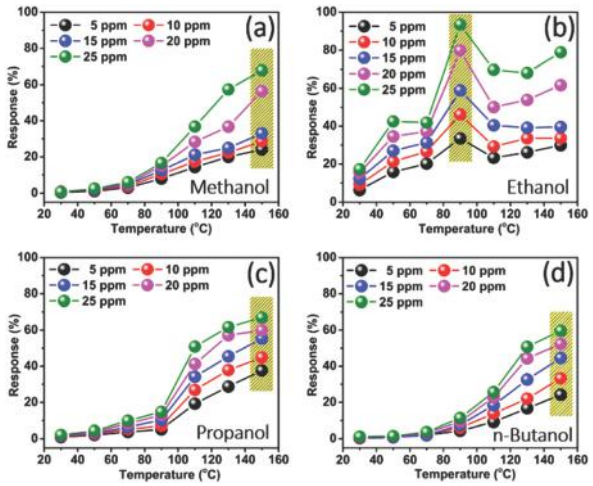

Fig. 5 (a–d) The sensing properties of the SnS_2 NLS sensor toward different VOCs.

temperature. Fig. 5(a)–(d) shows the VOC responses of the SnS_2 NLS sensor to various concentrations (5–25 ppm) of VOC at different operating temperatures (30–150 °C). Fig. S6(a)–(d) (ESI†) shows the resistance properties of the SnS_2 NLS sensor to different VOCs at various concentrations (5–25 ppm) and different operating temperatures (30–150 °C). It is observed that the SnS_2 gas sensor resistance varies as a function of the operating temperature. The responses of the SnS_2 NLS sensor increase with concentration and operating temperature toward all VOCs, except in the case of ethanol, where there is a high response of 93.5% at 90 °C which, after that, decreases and then increases again. The SnS_2 NLS sensor demonstrates a negligible response towards methanol ($\leq$5.9%), propanol ($\leq$9.9%), and *n*-butanol ($\leq$3.7%) at 25 ppm at temperature of $\leq$70 °C, as shown in Fig. 5(a), (c) and (d). However, there is a good response towards ethanol ($\leq$41.9%) at a concentration of 25 ppm at a similar operating temperature ($\leq$70 °C), as revealed in Fig. 5(b). The SnS_2 NLS sensor reveals the highest response to ethanol (93.5% at 90 °C) compared with methanol (67.9% at 150 °C), propanol (67.0% at 150 °C), and *n*-butanol (59.7% at 150 °C) at a concentration of 25 ppm, as shown in Fig. 5(a)–(d). Therefore, it is concluded that the SnS_2 NLS sensor manifests maximum responses towards VOCs at different operating temperatures. This may be due to the following reasons, which are subdivided into two operating temperature ranges ($\leq$70 °C and $\geq$90 °C). At low operating temperatures ($\leq$70 °C): (i) sparse interactions between less thermally excited conduction electrons and atmospheric oxygen form fewer active sites (O_2^-, O^-, and O^{2-}) on the SnS_2 NLS sensing material surface, causing slow interactions with VOC molecules, which results in a low response;[29] and (ii) a high concentration of VOC molecules on the SnS_2 NLS sensor surface with low adsorption/desorption rates and a substantial potential barrier is also another reason for the low response. In the high operating temperature range ($\geq$90 °C): (i) the high thermal energy supports valence electrons jumping into the conduction band, which leads to more interactions between thermally excited conduction electrons and atmospheric oxygen, with conversion into ionic active sites, resulting in quick response/recovery times; and (ii) the activation energy of surface reactions and the binding energy between VOC molecules and the SnS_2 NLS sensing material are more suitable in the case of ethanol (compared to methanol, propanol, and *n*-butanol), leading to the high response to this particular VOC.[30] Interestingly, the unique SnS_2 NLS leads to plentiful channels (as illustrated in Fig. 1(a)–(f) and 2(a)–(d)) and active sites (O_x^-) on the surface for VOC diffusion, adsorption, and chemisorption, which results in outstanding gas sensing performance toward VOCs (ethanol, methanol, propanol, and *n*-butanol).[30]

Fig. 6(a)–(d) exhibits the real-time response/recovery characteristics of the SnS_2 NLS sensor towards VOCs at various concentrations and different working temperatures. Moreover, Fig. S6(a)–(d) (ESI†) shows the resistance characteristics of the SnS_2 NLS sensor towards VOCs at various concentrations (5–25 ppm) and different working temperatures (30–150 °C). It is perceived that the response rises sharply as the target VOC concentration increases in the gas sensing test chamber, as shown in Fig. 6(a)–(d). However, the response recovers to its initial value after the VOC is liberated from the gas sensing test chamber upon the insertion of air. The response and recovery times are two salient features when examining the VOC sensing performance of the SnS_2 NLS VOC sensor. The VOC response and recovery times decrease with an increase in the target VOC concentration and operating temperature of the SnS_2 NLS sensor, as depicted in Fig. 6(a)–(d). Further, it is observed that the SnS_2 NLS sensor illustrates the highest and most rapid response and the sharpest recovery time in response to ethanol at a temperature of 90 °C, compared with methanol, propanol, and *n*-butanol, as demonstrated in Fig. 6(a)–(d).

The sensor exhibits slow response and recovery times at working temperatures of $\leq$70 °C for all VOCs; however, it manifests fast response and recovery times at working temperatures $\geq$90 °C because of the enhanced oxidation/reduction abilities of the VOC molecules.[31] Also, the recovery time is not commensurate

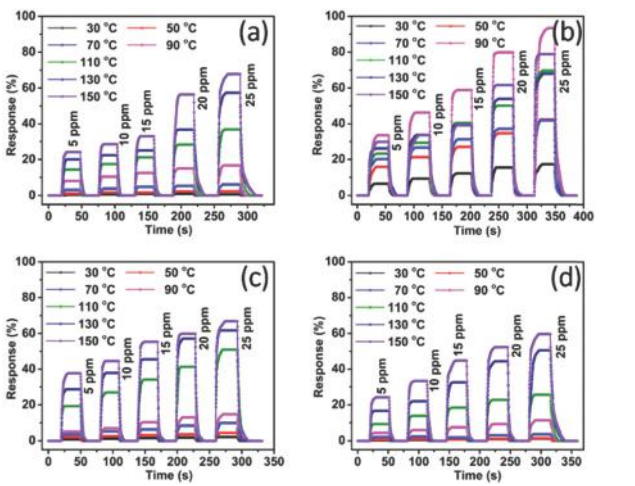

Fig. 6 The dynamic response/recovery characteristics toward (a) methanol, (b) ethanol, (c) propanol, and (d) *n*-butanol of the SnS_2 NLS sensor at various concentrations and different temperatures.

to the response speed; however, when the interactions of VOCs with the SnS_2 NLS sensing element in the test gas chamber are slow, this results in high response and recovery times. At $\geq$90 °C, the reduced response and recovery times may be due to the possible role of the high electrical conductivity of SnS_2 NLS, which accelerates electron transfer speeds on the surface of the VOC sensing material.[32] Also, high thermal energy can promote fast electron transfer rates, decreasing the response and recovery reaction potential barriers and delivering quick sensor response and recovery times toward VOCs at high operating temperatures of $\geq$90 °C. In addition, the nano/micropores, high surface area, and nano-lotus morphology of SnS_2 NLS provide excellent channels for the quick adsorption/desorption of VOC molecules, and the material is capable of stimulating analyte adsorption after overcoming a potential barrier, which can enhance the speeds of response and recovery reactions.[33] Further, SnS_2 NLS undergoes convenient lotus-petal-based reactions that show a reversible phenomenon. The surfaces with cone-shaped and curved faces, as illustrated in Fig. 1 and 2, facilitate better interactions between VOC molecules and the sensing material (lotus-petal networks), allowing fast and reversible adsorption kinetics toward VOCs with quick response and recovery times.[34] Moreover, the sensitivity to 25 ppm ethanol increased and reached a maximum; after that, it decreased when the operating temperature was increased further. This is attributed to dynamic equilibrium between the adsorption and desorption reactions involving ethanol molecules.[34]

Fig. 7 shows an illustration of the evaluation of the response and recovery times toward 25 ppm ethanol at 90 °C. The response time is described as the time taken for the SnS_2 NLS sensor to reach nearly 90% of its maximum response when the VOC is introduced into the gas chamber. Likewise, the recovery time is the time taken for the SnS_2 NLS sensor to recover 90% of its minimum response when the VOC is removed from the gas chamber.[27] From Fig. 7, the measured response and recovery times in response to 25 ppm ethanol are 14.2 s and 16.6 s, respectively, at 90 °C. It is also seen that the ethanol response and recovery times are fast compared with other VOCs, as revealed in Fig. 6(a)–(d). The response time depends on different factors, such as the VOC molecular weight and the operating temperature, which influence the chemical reactivity of a target gas with adsorbed oxygen species.[34]

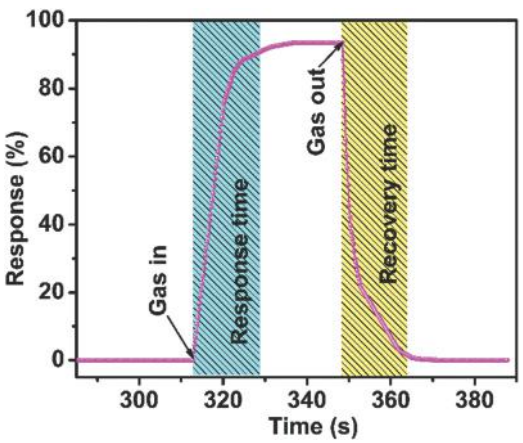

Fig. 7 An illustration of the response and recovery times of the SnS_2 NLS sensor toward 25 ppm ethanol at 90 °C.

Therefore, it is concluded from the response curves (Fig. 5) and dynamic response/recovery plots (Fig. 6) that the optimum operating temperatures for using the SnS_2 NLS sensor to detect 25 ppm concentrations of VOCs are 90 °C for ethanol, 150 °C for methanol, 150 °C for propanol, and 150 °C for *n*-butanol. As a result, the SnS_2 NLS sensor shows the highest response towards ethanol at a concentration of 25 ppm at a minimum operating temperature of 90 °C, as shown in Fig. 5 and 6. Accordingly, the optimum operating temperature of 90 °C and concentration of 25 ppm have been selected to examine two important parameters: the selectivity and stability of the SnS_2 NLS sensor. The selectivity of the SnS_2 NLS sensor toward VOCs is a vital parameter describing the discrimination and detection of the gas of interest at a particular working temperature and concentration. The gas response towards the VOC of interest is required to be noticeably higher than the responses toward other interfering gas at identical concentrations and operating temperatures for selective gas recognition.

In the present study, methanol, propanol, *n*-butanol, benzene, toluene, and *n*-butylacetate have been chosen as interfering gases to examine the selective nature of the SnS_2 NLS ethanol sensor. Fig. 8(a) shows the dynamic characteristics of the selectivity of the SnS_2 NLS ethanol sensor towards interfering gases, such as methanol, propanol, *n*-butanol, benzene, toluene, and *n*-butylacetate, at the optimized working temperature (90 °C) and a constant concentration of 25 ppm. In addition, Fig. S7(a) (ESI†) illustrates the real-time resistance characteristics of the SnS_2 NLS ethanol sensor towards interfering gases, such as methanol, propanol, *n*-butanol, benzene, toluene, and *n*-butylacetate, at 90 °C and a concentration of 25 ppm. The SnS_2 NLS sensor demonstrates better selectivity towards ethanol, with a response of 92.9%, compared with other interfering gases such as methanol (a response of 16.4%), propanol (a response of 14.8%), *n*-butanol (a response of 11.4%), benzene (a response of 4.1%), toluene (a response of 5.8%), and *n*-butylacetate (a response of 2.2%). Furthermore, the selectivity coefficient (S_c) values of the SnS_2 NLS sensor towards ethanol have been evaluated using eqn (S9) (ESI†), as discussed in the ESI,† and they are listed in Table S3 (ESI†).[35] The evaluated selectivity coefficient values for the SnS_2 NLS ethanol sensor are 5.7 for methanol, 6.3 for propanol, 8.1 for *n*-butanol, 22.7 for benzene, 16.0 for toluene, and 42.2 for *n*-butylacetate. The high value of selectivity with reference to *n*-butylacetate (42.2) indicates that the response of SnS_2 NLS to ethanol is 34.5 times higher than the response to *n*-butylacetate; however, the response is only around six times higher to ethanol than to methanol. The high selectivity of the SnS_2 NLS sensor towards ethanol compared with other interfering gases at 25 ppm and 90 °C may be due to the following reasons: (i) the high chemical reactivity of ethanol molecules with adsorbed oxygen species on the SnS_2 NLS sensor surface compared with other interfering gases;[35] (ii) the strong electronegativity of SnS_2 NLS and its efficient interactions with ethanol molecules compared with other gases;[11,12] and (iii) a higher rate

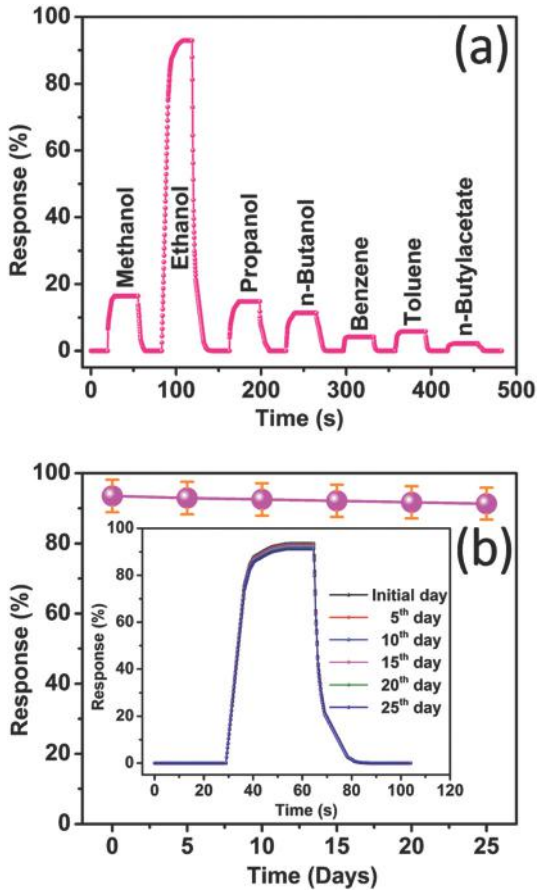

Fig. 8 (a) The selectivity for ethanol in the presence of various interfering gas and (b) stability testing in response to ethanol over twenty-five days (with measurements at five-day intervals) using the SnS_2 NLS sensor at concentrations of 25 ppm at 90 °C.

of ethanol molecule transfer to the SnS_2 NLS sensing layer, resulting in a quick response and high selectivity towards ethanol compared with other gases.[35] From Fig. 5, it is also observed that the SnS_2 NLS sensor showed the highest sensitivity towards ethanol at 90 °C, compared with methanol, propanol, and *n*-butanol at 150 °C. Therefore, we can say that SnS_2 NLS undergoes excellent and robust interactions with ethanol molecules compared with the other interfering gases at a low operating temperature of 90 °C, resulting in the highest selectivity being seen towards ethanol.

For commercialization, the long-term stability of the SnS_2 NLS sensor is also vital, as the VOC sensor must retain reliability during its service life. To examine the stability of the SnS_2 NLS ethanol sensor, response measurements were carried out at the optimum working temperature of 90 °C at a concentration of 25 ppm. Fig. 8(b) demonstrates the stability results of the SnS_2 NLS sensor at the optimum working temperature of 90 °C toward a fixed ethanol concentration of 25 ppm for 25 days of testing with gaps of 5 days between measurements. The inset in Fig. 8(b) shows the transient stability characteristics of the SnS_2 NLS sensor toward 25 ppm ethanol at 90 °C. Additionally, Fig. S7(b) (ESI†) elucidates the real-time resistance characteristics of the stability testing results shown in Fig. 8(b) for the SnS_2 NLS sensor at the optimum working temperature of 90 °C for a fixed ethanol concentration of 25 ppm. Fig. S7(b) (ESI†) shows the variations in the baseline resistance of the dynamic response during the 25 days of service, showing the excellent stability. It is also observed in Fig. S7(b) (ESI†) that the SnS_2 NLS sensor resistance varies from ~246.6 kΩ to ~252.5 kΩ from the first day to the 25th day. The SnS_2 NLS sensor offers excellent stability, with a response of 91.3% retained on day 25, showing a slight response reduction of 2.6% toward 25 ppm ethanol at 90 °C. The enduring nature of the SnS_2 NLS sensor can be attributed to the following aspects: (i) the morphology, lattice strain, and good conductivity of the VOC sensing material;[28] (ii) the low response and recovery barrier heights; and (iii) the existence of Urbach energy states below the conduction band, which boosted the chemisorption interactions between active sites on the surface of SnS_2 NLS and VOC molecules, as discussed relating to Fig. 4.

The SnS_2 NLS sensor demonstrated a higher response towards ethanol at 90 °C than other VOCs. Therefore, we calculated the theoretical ethanol detection limit at 90 °C. Fig. 9 shows the concentration-dependent response to ethanol of the SnS_2 NLS sensor (90 °C), which indicates the device's practical applicability. The theoretical detection limit (DL) can be calculated using eqn (2), as given below:[36]

$$\mathrm{DL} = 3\frac{\mathrm{rms}_{\mathrm{noise}}}{k} \quad (2)$$

where k is the slope of the logarithmic plot [Fig. 9], and $\mathrm{rms}_{\mathrm{noise}}$ is the root-mean-square deviation from the baseline of Fig. 6(b) at 90 °C. $\mathrm{rms}_{\mathrm{noise}}$ is calculated using eqn (3):

$$\mathrm{rms}_{\mathrm{noise}} = \sqrt{\frac{\sum (y - y_i)^2}{N}} \quad (3)$$

where y represents the baseline data points, y_i represents the averages of baseline data points, and N is the number of data points (here, we used ten data points). Therefore, the calculated detection limit of the SnS_2 NLS ethanol sensor is 7.9 ppb at 90 °C.

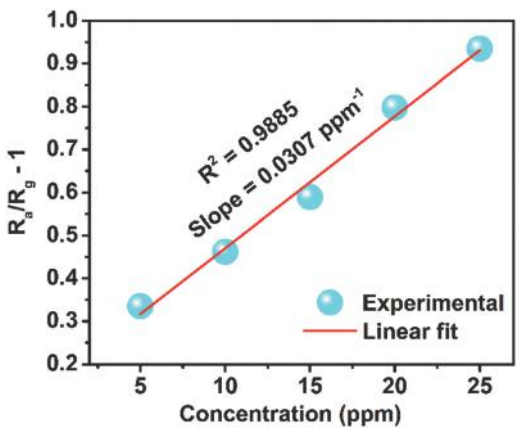

Fig. 9 A plot of the ethanol response *vs.* concentration for the SnS_2 NLS sensor at 90 °C.

Gas sensing mechanism

Here, we used the SnS_2 nano-lotus structure (NLS) to describe the gas sensing mechanism, and in a similar way, this can be applied to the entire sensor surface. When the SnS_2 NLS VOC sensor is exposed to ambient air, oxygen is chemisorbed on the SnS_2 NLS surface (as illustrated in eqn (4)–(7)), which further entraps electrons in the conduction band of SnS_2 to form ionic species (O_x^-), such as O_2^-, O^-, and O^{2-}, as articulated in Fig. 10(a), (d), and (g). The chemisorbed atmospheric oxygen species exist around the grains, grain boundaries, and surface of SnS_2 NLS, leading to an electron depletion layer and potential barrier height, as divulged schematically in Fig. 10(b), (e) and (c), (f). A higher reaction potential barrier height hampers electron transport between grains, resulting in decreased SnS_2 NLS conductivity.[37]

The interactions between atmospheric oxygen and the sensor surface in the reaction mechanism can be written as shown in eqn (4)–(7):[38,39]

$$O_2\ (gas) \rightarrow O_2\ (ads) \quad (4)$$

$$O_2\ (ads) + e^- \rightarrow O_2^- \quad (5)$$

$$O_2^-\ (ads) + e^- \rightarrow 2O^- \quad (6)$$

$$O^-\ (ads) + e^- \rightarrow O^{2-} \quad (7)$$

The reaction mechanism provided above and the formation of ionic active sites on the SnS_2 NLS sensor surface are visualized graphically in Fig. 10(a)–(c). The VOC molecules diffuse on the surface of the sensing element, SnS_2 NLS, when the VOC is inserted into the test gas chamber. After that, the VOC

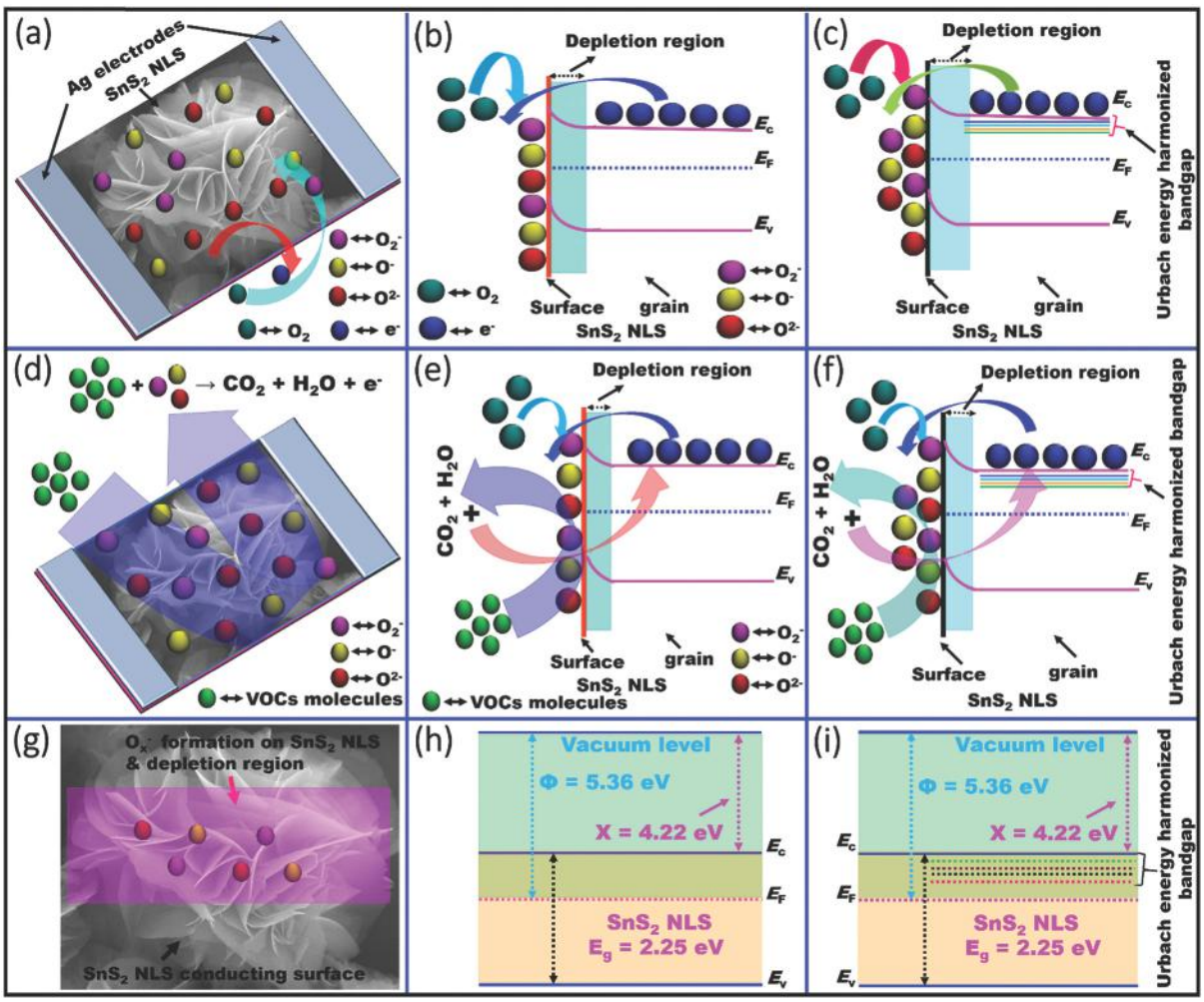

Fig. 10 A schematic representation of the VOC sensing mechanism of the SnS_2 NLS sensor: (a) the adsorption of O_2 on the SnS_2 surface, taking electrons from the SnS_2 sensing element; the concepts of the formation of (b) the depletion region when the SnS_2 sensor is exposed to air and (c) the depletion region in the Urbach energy harmonized bandgap; (d) a visualization of the interactions between VOC molecules and the ionic active sites (O_x^-) on the SnS_2 surface; the concepts of the reduction of the depletion region and the transfer of electrons into the conduction band of SnS_2 during VOC sensing (e) without the Urbach energy harmonized bandgap and (f) with the Urbach energy harmonized bandgap; (g) the concept of the adsorption of active sites and the formation of the depletion region on the surface of SnS_2; and illustrations of the work function and electron affinity (h) without and (i) with the concept of the Urbach energy harmonized nano-lotus SnS_2 bandgap.

molecules disintegrate into carbon dioxide (CO_2) and water molecules (H_2O) *via* ions adsorbed on the SnS_2 NLS surface, with the return of trapped electrons back to the conduction band, as schematically represented in Fig. 10(d)–(f). The generalized form of the reaction mechanism of VOCs with the adsorbed active ions (O_x^-) on the surface of SnS_2 NLS can be illustrated in eqn (8) and (9):[39]

$$\text{VOC (gas)} \leftrightarrow \text{VOC (ads)} \quad (8)$$

$$\text{VOC (ads)} + O_x^- \rightarrow CO_2 + H_2O + e^- \quad (9)$$

The adsorbed active ion species (O_x^-) utilized in reactions with VOCs, as discussed in eqn (8) and (9), result in a reduced reaction potential barrier, which encourages the transfer of electrons from one grain to another, resulting in the increased conductivity of the SnS_2 NLS sensor element, as expressed *via* the graphical visualization in Fig. 10(d)–(f).

Furthermore, possible reaction mechanisms between individual VOC types and adsorbed oxygen species (O^-) are shown in eqn (10)–(13):[40–43]

$$CH_3OH\ (ads) + 3O^-\ (ads) \rightarrow CO_2 + 2H_2O + 3e^- \quad (10)$$

$$C_2H_5OH\ (ads) + 6O^-\ (ads) \rightarrow 2CO_2 + 3H_2O + 6e^- \quad (11)$$

$$CH_3CHOHCH_3\ (ads) + 9O^-\ (ads) \rightarrow 3CO_2 + 4H_2O + 9e^- \quad (12)$$

$$C_2H_9OH\ (ads) + 12O^-\ (ads) \rightarrow 4CO_2 + 5H_2O + 12e^- \quad (13)$$

It is observed that VOCs react with adsorbed oxygen species (O^-) and are converted into carbon dioxide and water molecules, releasing electrons into the conduction band of the SnS_2 NLS sensing material.

In addition to the above-discussed VOC sensing mechanism, the ionic active sites and interactions between the ionic active sites and the VOC molecules were investigated. Fig. 10 illustrates a schematic presentation of the proposed VOC sensing mechanism. Fig. 10(a)–(c) visualizes the concept of the adsorption of atmospheric oxygen (O_2) and the formation of ionic active sites (O_x^-) on the surface of SnS_2 NLS (as discussed in eqn (4)–(7)), and the concept of the harmonized bandgap due to lattice strain, the slight reduction in lattice parameters ($a = b$, and c), and the lattice spacing, as discussed above and listed in Table S1 (ESI†). Fig. 10(b) and (c) shows the formation of the electron depletion region during the adsorption/desorption of ionic active sites on the SnS_2 NLS sensor surface; the existence of Urbach energy states harmonizes the optical bandgap of SnS_2 NLS and encourages more electrons to interact with O_2.

Fig. 10(d) unveils the interactions of VOC molecules with adsorbed ionic active sites on the sensor surface, *via* a realistic conceptualized view of SnS_2 NLS, liberating carbon dioxide and water molecules and releasing electrons back into the conduction band. Fig. 10(e) and (f) elucidates the interactions between VOC molecules and the adsorbed ionic sites on the surface of the SnS_2 NLS sensor, which modulate the electron depletion region and also the potential barrier height in cases both without and with an Urbach-energy-state-harmonized bandgap. Fig. 10(f) shows the increased electron depletion region and potential barrier height in the presence of Urbach energy states below the conduction band, leading to a faster electron transfer rate for interacting with O_2 and forming more ionic active sites (O_x^-) compared to the case without Urbach energy states shown in Fig. 10(e). Further, the Urbach energy states allow the expansion of the conduction pathways for electrons to flow between SnS_2 NLS grains, which results in high conductivity and outstanding gas sensing properties upon exposure to VOCs in the test gas chamber.[44]

Giving a top-view demonstration, Fig. 10(g) shows the formation of ionic active sites on the conductive surface of the SnS_2 NLS sensor and the development of the depletion region. Interestingly, the optical bandgap (2.25 eV) and Urbach energy states of SnS_2 NLS are discussed and illustrated in Fig. 4(a) and (b). The work function and electron affinity of SnS_2 NLS are 5.36 eV and 4.22 eV, respectively.[45,46] Therefore, the band diagram of SnS_2 NLS can be drawn including the positions of the valence band maximum and conduction band minimum, as shown in Fig. 10(h). Fig. 10(i) shows the existence of Urbach energy states under the conduction band minimum in the energy band diagram of SnS_2 NLS, which can further boost electron transfer rate (thermal fluctuations linked with SnS_2 lattice phonons) to enhance the chemisorption process during VOC sensing.

Table 1 A comparison of the ethanol sensing properties of the SnS_2 NLS VOC sensor with other SnS_2- and metal-oxide-based ethanol sensors reported in the literature

Sensor element	Operating temperature (°C)	Concentration (ppm)	Test gas	Response	Selectivity	Stability	Response time (s)	Recovery time (s)	Ref.
SnS_2 nano-lotus	90	25	Ethanol	93.5%	Yes	91.3% (25 days)	14.2	16.6	This work
SnS_2	25	150	Ethanol	<150	Yes	No	~66	~42	16
SnS/SnS_2	200	100	Ethanol	30.1	Yes	96.7% (16 days)	~60	~20	17
SnS	160	100	Ethanol	14.9	Yes	Yes (five cycles; <14 min)	23	26	18
SnS_2	25	800	Ethanol	<30%	No	No	69	57	19
MoS_2/ZnO	220	500	Ethanol	12.08	No	Yes (five cycles; ~550 min)	30	10	50
WS_2	30	500	Ethanol	90.3	No	No	~7	~5	51
MoS_2/pSi	30	10	Ethanol	7.3	Yes	7.1% (60 days)	~55	~43	52
In-Doped 3D ZnO	250	100	Ethanol	~88	Yes	Yes (several cycles; ~3500 min)	25	10	53
SnO_2/Zn_2SnO_4	250	100	Ethanol	30.5	Yes	~28.6% (20 days)	~82	~43	54

Response formula used: $[(R_a - R_g)/R_g] \times 100\%$ (this work, ref. 16 and 19); R_a/R_g;[17,18,50,51,53,54] $[(R_{analyte} - R_{air})/R_{air}] \times 100\%$.[52]

Further, the Urbach energy states represent structural and thermal disorder or Frenkel exciton interactions with the lattice vibrations of the SnS_2 semiconductor or the role of lattice defects (lattice strain, as discussed relating to the XRD analysis in Table S1, ESI†) fueled by phonons in determining the optical characteristics of SnS_2 NLS.[47–49] Moreover, the Urbach energy can also be envisioned as a shared effect of thermal fluctuations (linked with SnS_2 lattice phonons), lattice strain, and impurities on the valence band and conduction band edges.[49]

Table 1 illustrates a comparison between the SnS_2 NLS VOC sensor (present work) and other reported VOC gas sensors based on SnS_2, SnS/SnS_2, SnS, MoS_2/ZnO, WS_2, MoS_2/pSi, In-doped 3D ZnO, and SnO_2/Zn_2SnO_4. The response and recovery times of the SnS_2 NLS VOC sensor are 14.2 s and 16.6 s, respectively, comparing favorably with other reported results for SnS_2 (66 s/42 s),[16] SnS/SnS_2 (60 s/20 s),[17] SnS (23 s/26 s),[18] SnS_2 (69 s/57 s),[19] MoS_2/ZnO (30 s/10 s),[50] WS_2 (7 s/5 s),[51] MoS_2/pSi (55 s/43 s),[52] In-doped 3D ZnO (25 s/10 s),[53] and SnO_2/Zn_2SnO_4 (82 s/43 s).[54] The SnS_2 NLS VOC sensor demonstrated high durability compared with other reported studies. Also, the SnS_2 NLS VOC sensor revealed high sensitivity at a low VOC sensing concentration (93.5% at 25 ppm) compared with other reported sensors such as SnS_2 (150 at 150 ppm),[16] SnS/SnS_2 (30.1 at 100 ppm),[17] SnS (14.9 at 100 ppm),[18] SnS_2 (30% at 800 ppm),[19] MoS_2/ZnO (12.08 at 500 ppm),[50] WS_2 (90.3 at 500 ppm),[51] MoS_2/pSi (20% at 40 ppm),[52] In-doped 3D ZnO (88 at 100 ppm),[53] and SnO_2/Zn_2SnO_4 (30.5 at 100 ppm).[54] Therefore, it can be concluded that the SnS_2 NLS sensor shows excellent VOC sensing properties, and it can be useful as a VOC sensor for driving safety and the prevention of traffic accidents due to drunk driving.

Conclusions

SnS_2 NLS is developed successfully in this research for the fabrication of a highly selective, sensitive, and stable gas sensor for the detection of VOCs (5–25 ppm) at different operating temperatures (30–150 °C). The SnS_2 NLS sensor exhibited fast response and recovery times (14.2 s and 16.6 s), good selectivity (92.9%), and outstanding stability (a response of 91.3% after 25 days) toward ethanol. It also shows quick response and recovery dynamics, which can be further described based on the Urbach energy harmonized optical bandgap of SnS_2 NLS. In addition, the SnS_2 NLS sensor was used in a comparative study of VOC sensing, and it showed the highest response towards ethanol out of a selection of VOCs. Overall, this efficient and affordable VOC sensor, showing 3-S features, is suitable for promotion due to its tunable performance and the need for practical sensors for indoor air quality assessment, ethanol detection by federal agencies to protect against drunken driving, *etc.*

Conflicts of interest

There are no conflicts to declare.

Acknowledgements

This work was supported through the Basic Science Research Program through the National Research Foundation of Korea (NRF), funded by the Ministry of Science, ICT, and Future Planning (Grant No. 2019R1D1A3A03103662).

Notes and references

1 Y. He, D. Li, W. Gao, H. Yin, F. Chen and Y. Sun, High-performance NO_2 sensors based on spontaneously functionalized hexagonal boron nitride nanosheets via chemical exfoliation, *Nanoscale*, 2019, **11**, 21909–21916.
2 Z. Feng, Y. Ma, V. Natarajan, Q. Zhao, X. Ma and J. Zhan, In-situ generation of highly dispersed Au nanoparticles on porous ZnO nanoplates via ion exchange from hydrozincite for VOCs gas sensing, *Sens. Actuators, B*, 2018, **255**, 884–890.
3 G. Ingrosso, Free radical chemistry and its concern with indoor air quality: an open problem, *Microchem. J.*, 2002, **73**, 221–236.
4 M. Kadosaki, Y. Sakai, I. Tamura, I. Matsubara and T. Itoh, Development of an Oxide Semiconductor Thick Film Gas Sensor for the Detection of Total Volatile Organic Compounds, *Electron. Commun. Jpn.*, 2010, **93**, 34–41.
5 H. Kim, J. Singh, Y. N. Yun, M. Sohail, T. W. Kim, J. Y. Lee, W. Choi and D. Kim, Metal−Organic Framework-Derived MgO/$Mg(OH)_2$@Nanoporous Carbon for High Thermal Energy Release, *ACS Appl. Nano Mater.*, 2020, **3**, 3295–3304.
6 Z. Wang, Z. Tian, D. Han and F. Gu, Au-modified three-dimensionally ordered macroporous ZnO:In for high-performance ethanol sensors, *J. Mater. Chem. C*, 2020, **8**, 2812–2819.
7 Q. Zhang, F. Meng, L. Zha, X. Wang and G. Zhang, A sensitive cataluminescence-based sensor using a $SrCO_3$/graphene composite for n-propanol, *RSC Adv.*, 2015, **5**, 57482–57489.
8 T. T. Tung, M. T. Tran, J.-F. Feller, M. Castro, T. V. Ngo, K. Hassan, M. J. Nine and D. Losic, Graphene and metal organic frameworks (MOFs) hybridization for tunable chemoresistive sensors for detection of volatile organic compounds (VOCs) biomarkers, *Carbon*, 2020, **159**, 333–344.
9 J. D. Pleil, M. A. Stiegel and T. H. Risby, Clinical breath analysis: discriminating between human endogenous compounds and exogenous (environmental) chemical confounders, *J. Breath Res.*, 2013, **7**, 017107.
10 D. Voiry, J. Yang and M. Chhowalla, Recent Strategies for Improving the Catalytic Activity of 2D TMD Nanosheets Toward the Hydrogen Evolution Reaction, *Adv. Mater.*, 2016, **28**, 6197–6206.
11 S. R. Damkale, S. S. Arbuj, G. G. Umarji, R. P. Panmand, S. K. Khore, R. S. Sonawane, S. B. Rane and B. B. Kale, Two-dimensional hexagonal SnS_2 nanostructures for photocatalytic hydrogen generation and dye degradation, *Sustainable Energy Fuels*, 2019, **3**, 3406–3414.
12 T. Feng, D. Zhang, X. Li, Q. Abdul, Z. Shi, J. Lu, P. Guo, Y. Zhang, J. Liu and Q. J. Wang, SnS_2 Nanosheets for

Er-Doped Fiber Lasers, *ACS Appl. Nano Mater.*, 2020, **3**, 674–681.

13 H. Chang, E. In, K.-J. Kong, J.-O. Lee, Y. Choi and B.-H. Ryu, First-Principles Studies of SnS_2 Nanotubes: A Potential Semiconductor Nanowire, *J. Phys. Chem. B*, 2005, **109**, 30–32.

14 D. Thangaraju, R. Marnadu, V. Santhana, A. Durairajan, P. Kathirvel, J. Chandrasekaran, S. Jayakumar, M. A. Valente and D. C. Greenidge, Solvent influenced synthesis of single-phase SnS_2 nanosheets for solution-processed photodiode fabrication, *CrystEngComm*, 2020, **22**, 525–533.

15 (*a*) Q. Sun, J. Wang, J. Hao, S. Zheng, P. Wan, T. Wang, H. Fang and Y. Wang, SnS_2/SnS p–n heterojunctions with an accumulation layer for ultrasensitive room-temperature NO_2 detection, *Nanoscale*, 2019, **11**, 13741–13749; (*b*) T. Shimada, F. S. Ohuchi and B. A. Parkinson, Thermal decomposition of SnS_2 and $SnSe_2$: Novel molecular-beam epitaxy sources for sulfur and selenium, *J. Vac. Sci. Technol., A*, 1992, **10**, 539–542.

16 L. D. Bharatula, M. B. Erande, I. S. Mulla, C. S. Rout and D. J. Late, SnS_2 nanoflakes for efficient humidity and alcohol sensing at room temperature, *RSC Adv.*, 2016, **6**, 105421.

17 Q. X. Zhang, S. Y. Ma, R. Zhang, Y. Tie and S. T. Pei, Optimization ethanol detection performance manifested by SnS/SnS_2 nanoparticles, *Mater. Lett.*, 2020, **258**, 126783.

18 W. Shan, Z. Fu, M. Ma, Z. Liu, Z. Xue, J. Xu, F. Zhang and Y. Li, Facile Chemical Bath Synthesis of SnS Nanosheets and Their Ethanol Sensing Properties, *Sensors*, 2019, **19**, 2581.

19 P. S. Kuchi, H. Roshan and M. H. Sheikhi, A novel room temperature ethanol sensor based on PbS:SnS_2 nanocomposite with enhanced ethanol sensing properties, *J. Alloys Compd.*, 2020, **816**, 152666.

20 L. Fan, X. Li, X. Song, N. Hu, D. Xiong, A. Koo and X. Sun, Promising Dual-Doped Graphene Aerogel/SnS_2 Nanocrystal Building High Performance Sodium Ion Batteries, *ACS Appl. Mater. Interfaces*, 2018, **10**, 2637–2648.

21 T. Billo, I. Shown, A. K. Anbalagan, T. A. Effendi, A. Sabbah, F.-Y. Fu, C.-M. Chu, W.-Y. Woon, R.-S. Chen, C.-H. Lee, K.-H. Chen and L.-C. Chen, A mechanistic study of molecular CO_2 interaction and adsorption on carbon implanted SnS_2 thin film for photocatalytic CO_2 reduction activity, *Nano Energy*, 2020, **72**, 104717.

22 Y. Zhang, P. Zhu, L. Huang, J. Xie, S. Zhang, G. Cao and X. Zhao, Few-Layered SnS_2 on Few-Layered Reduced Graphene Oxide as Na-Ion Battery Anode with Ultralong Cycle Life and Superior Rate Capability, *Adv. Funct. Mater.*, 2015, **25**, 481–489.

23 C. Wu, D. Guo, P. Li, S. Wang, A. Liu and F. Wu, A study on the effects of mixed organic cations on the structure and properties in lead halide perovskites, *Phys. Chem. Chem. Phys.*, 2020, **22**, 3105–3111.

24 J. Torrent and V. Barron, Diffuse Reflectance Spectroscopy of Iron Oxides, Encycl, *Surf. Colloid Sci.*, 2002, 1438–1446.

25 S. B. Upadhyay, R. K. Mishra and P. P. Sahay, Enhanced acetone response in co-precipitated WO_3 nanostructures upon indium doping, *Sens. Actuators, B*, 2015, **209**, 368–376.

26 (*a*) P. Chetri and A. Choudhury, Investigation of optical properties of SnO_2 nanoparticles, *Physica E*, 2013, **47**, 257–263; (*b*) S. Roy, A. G. Joshi, S. Chattergee and A. K. Ghosh, Local symmetry breaking in SnO_2 nanocrystals with cobalt doping and its effect on optical properties, *Nanoscale*, 2018, **10**, 10664–10682.

27 (*a*) R. K. Mishra, S. B. Upadhyay, A. Kushwaha, T.-H. Kim, G. Murali, R. Verma, M. Srivastava, J. Singh, P. P. Sahay and S. H. Lee, SnO_2 quantum dots decorated on RGO: a superior sensitive, selective and reproducible performance for a H_2 and LPG sensor, *Nanoscale*, 2015, **7**, 11971–11979; (*b*) Y. Zhao, J.-G. Song, G. H. Ryu, K. Y. Ko, W. J. Woo, Y. Kim, D. Kim, J. H. Lim, S. Lee, Z. Lee, J. Park and H. Kim, Low-temperature synthesis of 2D MoS_2 on a plastic substrate for a flexible gas sensor, *Nanoscale*, 2018, **10**, 9338–9345.

28 Y. Wang, P. Cheng, X. Li, C. Wang, C. Feng and G. Lu, Revealing the relationship between the Au decoration method and the enhanced acetone sensing performance of a mesoporous In_2O_3-based gas sensor, *J. Mater. Chem. C*, 2020, **8**, 78–88.

29 W.-Z. Li, M.-R. Wu, C.-Y. Tung, C.-Y. Huang, C.-S. Tan, Y.-S. Huang, L.-J. Chen and R.-H. Horng, Strain Control of a NO Gas Sensor Based on Ga-Doped ZnO Epilayers, *ACS Appl. Electron. Mater.*, 2020, **2**, 1365–1372.

30 (*a*) L. Sun, B. Wang and Y. Wang, High-Temperature Gas Sensor Based on Novel Pt Single Atoms@SnO_2 Nanorods@SiC Nanosheets Multi-heterojunctions, *ACS Appl. Mater. Interfaces*, 2020, **12**, 21808–21817; (*b*) Z. Song, Z. Huang, J. Liu, Z. Hu, J. Zhang, G. Zhang, F. Yi, S. Jiang, J. Lian, J. Yan, J. Zang and H. Liu, Fully Stretchable and Humidity-Resistant Quantum Dot Gas Sensors, *ACS Sens.*, 2018, **3**, 1048–1055.

31 J. Zhao, M. Hu, Y. Liang, Q. Li, X. Zhang and Z. Wang, A room temperature sub-ppm NO_2 gas sensor based on WO_3 hollow spheres, *New J. Chem.*, 2020, **44**, 5064–5070.

32 C. Wang, Y. Zhang, X. Sun, Y. Sun, F. Liu, X. Yan, C. Wang, P. Sun and G. Lu, Fast detection of alcohols by novel sea cucumber-like indium tungsten oxide, *Sens. Actuators, B*, 2020, **319**, 128158.

33 (*a*) L. Ma, X. Zhang, J. Wang, M. Ikram, M. Ullah, H. Lv, H. Wu and K. Shi, Controllable synthesis of an intercalated SnS_2/aEG structure for enhanced NO_2 gas sensing performance at room temperature, *New J. Chem.*, 2020, **44**, 8650–8659; (*b*) R. Malik, V. K. Tomar, Y. K. Mishra and L. Lin, Functional gas sensing nanomaterials: A panoramic view, *Appl. Phys. Rev.*, 2020, **7**, 021301; (*c*) A. Kaushik, R. Kumar, S. K. Arya, M. Nair, B. D. Malhotra and S. Bhansali, Organic–Inorganic Hybrid Nanocomposite-Based Gas Sensors for Environmental Monitoring, *Chem. Rev.*, 2015, **115**, 4571–4606.

34 (*a*) P. Wan, X. Wen, C. Sun, B. K. Chandran, H. Zhang, X. Sun and X. Chen, Flexible Transparent Films Based on Nanocomposite Networks of Polyaniline and Carbon Nanotubes for High-Performance Gas Sensing, *Small*, 2015, **11**, 5409–5415; (*b*) Z. Song, H. Chen, S. Bao, Z. Xie, Q. Kuang and L. Zheng, Nanosheet-assembled, hollowed-out hierarchical γ-Fe_2O_3 microrods for high-performance gas sensing, *J. Mater. Chem. A*, 2020, **8**, 3754–3762; (*c*) M. Vrnata, V. Myslık, F. Vyslouzl, M. Jelınek, J. Lancok and J. Zemek, The response of tin acetylacetonate and tin dioxide-based gas sensors to hydrogen and alcohol vapours, *Sens. Actuators, B*, 2000, **71**, 24–30.

35 (*a*) M. Siemons and U. Simon, Gas sensing properties of volume-doped $CoTiO_3$ synthesized via polyol method, *Sens. Actuators, B*, 2007, **126**, 595–603; (*b*) A. Umar, A. A. Ibrahim, H. Y. Ammar, U. T. Nakate, H. B. Albargi and Y. B. Hahn, Urchin like CuO hollow microspheres for selective high response ethanol sensor application: Experimental and theoretical studies, *Ceram. Int.*, 2021, **47**, 12084–12095; (*c*) M. Ghazi, S. Janfaza, H. Tahmooressi, A. Ravishankara, E. Earl, N. Tasnim and M. Hoorfar, Enhanced selectivity of microfluidic gas sensors by modifying microchannel geometry and surface chemistry with graphene quantum dots, *Sens. Actuators, B*, 2021, **342**, 130050.

36 (*a*) Y. G. Song, I. Jung, J. Shin, Y.-S. Shim, G. S. Kim, B.-K. Ju and C.-Y. Kang, Ionic-activated semiconducting gas sensors operated by piezoelectric generators at room temperature, *Sens. Actuators, B*, 2021, **332**, 129481; (*b*) L. Peng, Q. Zhao, D. Wang, J. Zhai, P. Wang, S. Pang and T. Xie, Ultraviolet-assisted gas sensing: A potential formaldehyde detection approach at room temperature based on zinc oxide nanorods, *Sens. Actuators, B*, 2009, **136**, 80–85.

37 W. Liu, Y. Xie, T. Chen, Q. Lu and S. U. Rehman, and Ling Zhua, Rationally designed mesoporous In_2O_3 nanofibers functionalized Pt catalysts for high-performance acetone gas sensors, *Sens. Actuators, B*, 2019, **298**, 126871.

38 N. H. Hanh, L. V. Duy, C. M. Hung, N. V. Duy, Y.-W. Heo, N. V. Hieu and N. D. Hoa, VOC gas sensor based on hollow cubic assembled nanocrystal Zn_2SnO_4 for breath analysis, *Sens. Actuators, A*, 2020, **302**, 111834.

39 X. Xing, Y. Yang, Z. Yan, Y. Hu, T. Zou, Z. Wang and Y. Wang, CdO-Ag-ZnO nanocomposites with hierarchically porous structure for effective VOCs gas-sensing properties, *Ceram. Int.*, 2019, **45**, 4322–4334.

40 Y. Zeng, Z. Hua, X. Tian, X. Li, Z. Qiu, C. Zhang, M. Wang and E.-P. Li, Selective detection of methanol by zeolite/Pd-WO_3 gas sensors, *Sens. Actuators, B*, 2018, **273**, 1291–1299.

41 (*a*) L. Zhu, Y. Wang, D. Zhang, C. Li, D. Sun, S. Wen, Y. Chen and S. Ruan, Gas Sensors Based on Metal Sulfide $Zn_{1-x}Cd_xS$ Nanowires with Excellent Performance, *ACS Appl. Mater. Interfaces*, 2015, **7**, 20793–20800; (*b*) O. Lupan, V. Cretu, V. Postica, N. Ababii, O. Polonskyi, V. Kaidas, F. Schutt, Y. K. Mishra, E. Monaico, I. Tiginyanu, V. Sontea, T. Strunskus, F. Faupel and R. Adelung, Enhanced ethanol vapour sensing performances of copper oxide nanocrystals with mixed phases, *Sens. Actuators, B*, 2016, **224**, 434–448.

42 Y. Yin, Y. Shen, P. Zhou, R. Lu, A. Li, S. Zhao, W. Liu, D. Wei and K. Wei, Fabrication, characterization and n-propanol sensing properties of perovskite-type $ZnSnO_3$ nanospheres based gas sensor, *Appl. Surf. Sci.*, 2020, **509**, 145335.

43 W. Li, Y. Ren and Y. Guo, ZrO_2/ZnO nanocomposite materials for chemiresistive butanol sensors, *Sens. Actuators, B*, 2020, **308**, 127658.

44 Y. Xu, L. Zheng, C. Yang, W. Zheng, X. Liu and J. Zhang, Chemiresistive sensors based on core-shell ZnO@TiO_2 nanorods designed by atomic layer deposition for n-butanol detection, *Sens. Actuators, B*, 2020, **310**, 127846.

45 J. Kim, J. Kim, S. Yoon, J.-Y. Kang, C.-W. Jeon and W. Jo, Single Phase Formation of SnS Competing with SnS_2 and Sn_2S_3 for Photovoltaic Applications: Optoelectronic Characteristics of ThinFilm Surfaces and Interfaces, *J. Phys. Chem. C*, 2018, **122**, 3523–3532.

46 L. A. Burton, T. J. Whittles, D. Hesp, W. M. Linhart, J. M. Skelton, B. Hou, R. F. Webster, G. O'Dowd, C. Reece, D. Cherns, D. J. Fermin, T. D. Veal, V. R. Dhanak and A. Walsh, Electronic and optical properties of single crystal SnS_2: an earth-abundant disulfide photocatalyst, *J. Mater. Chem. A*, 2016, **4**, 1312–1318.

47 A. Ates, M. A. Yildrim, M. Kundakci and M. Yildrim, Investigation of Optical and Structural Properties of CdS Thin Films, *Chin. J. Phys.*, 2007, **45**, 135–141.

48 J. Singh, Line shape of the low-energy tail of exciton absorption in molecular crystals, *Phys. Rev. B: Condens. Matter Mater. Phys.*, 1981, **23**, 2011–2021.

49 A. Podborska, B. Gaweł, Ł. Pietrzak, I. B. Szymanska, J. K. Jeszka, W. Łasocha and K. Szaciłowski, Anomalous Photocathodic Behavior of CdS within the Urbach Tail Region, *J. Phys. Chem. C*, 2009, **113**, 6774–6784.

50 Z. Song, J. Zhang and J. Jiang, Morphological evolution, luminescence properties and a high-sensitivity ethanol gas sensor based on 3D flower-like MoS_2-ZnO micro/nanospheres arrays, *Ceram. Int.*, 2020, **46**, 6634–6640.

51 S. Cao, Preparation of embedded circular disk and balls-like WS_2 nano/microstructures, photocatalytic properties and exposure to ethanol gas, *Mater. Lett.*, 2016, **185**, 460–463.

52 P. Dwivedi, S. Das and S. Dhanekar, Wafer-Scale Synthesized MoS_2/Porous Silicon Nanostructures for Efficient and Selective Ethanol Sensing at Room Temperature, *ACS Appl. Mater. Interfaces*, 2017, **9**, 21017–21024.

53 Z. Wang, Z. Tian, D. Han and F. Gu, Highly Sensitive and Selective Ethanol Sensor Fabricated with InDoped 3DOM ZnO, *ACS Appl. Mater. Interfaces*, 2016, **8**, 5466–5474.

54 X. Yang, H. Li, T. Li, Z. Li, W. Wu, C. Zhou, P. Sun, F. Liu, X. Yan, Y. Gao, X. Liang and G. Lu, Highly efficient ethanol gas sensor based on hierarchical SnO_2/Zn_2SnO4 porous spheres, *Sens. Actuators, B*, 2019, **282**, 339–346.